

Long-range current-induced spin accumulation in chiral crystals

Arunesh Roy,¹ Frank T. Cerasoli,^{2,*} Anooja Jayaraj,^{2,*}
Karma Tenzin,^{1,3,*} Marco Buongiorno Nardelli,^{2,4} and Jagoda Sławińska^{1,†}

¹Zernike Institute for Advanced Materials, University of Groningen, Nijenborgh 4, 9747AG Groningen, Netherlands

²Department of Physics, University of North Texas, Denton, TX 76203, USA

³Department of Physical Science, Sherubtse College,
Royal University of Bhutan, 42007 Kanglung, Trashigang, Bhutan

⁴The Santa Fe Institute, Santa Fe, NM 87501, USA

(Dated: March 11, 2022)

The chirality-induced spin selectivity (CISS) refers to a conversion between charge and spin currents occurring in chiral molecules and solids, which reveals a great potential for applications in various areas of technology. Nevertheless, after two decades of studies, the understanding of its microscopic origin remains elusive. Here, the CISS effect in materials with strong spin-orbit coupling is explained in terms of the unconventional current-induced spin accumulation, an analog of the Rashba-Edelstein effect that may manifest in systems with a radial spin texture reversing the sign for opposite enantiomers. The calculations of spin accumulation based on the density functional theory, performed for the first time for Te and TaSi₂, provide a rationale for the experimental studies reporting CISS in these materials. The analysis of a general Weyl-type spin-orbit coupling locally describing the spin texture at specific momentum vectors, reveals that a quasi-persistent spin helix emerges in the real space as a consequence of the crystal symmetries, and prevents the spins from decoherence, which qualitatively supports the observation of the long-range spin transport in CISS experiments. These results open the perspectives for DFT calculations of CISS for any chiral crystals and represent a step forward to its understanding in general systems.

Introduction. Several phenomena in nature are governed by the geometric property called chirality. It refers to any objects that are mirror reflections of each other and cannot be exactly superimposed by simple rotational or translational symmetry operations. Chiral objects such as molecules and crystals, similarly to human hands, have distinguishable right-handed and left-handed enantiomers which may manifest dissimilar physical and chemical properties and behave differently in response to external stimuli.¹⁻⁴ Among the variety of chirality-dependent phenomena, the chirality-induced spin selectivity (CISS) describing the generation of a collinear spin current by a charge current flowing through a chiral medium, is one of the most intriguing.⁵⁻⁷ It holds a great promise for various applications in electrochemistry,⁸ biorecognition,⁹ and spintronics,¹⁰⁻¹⁴ but a convincing explanation of its mechanism is still lacking.

While CISS is usually associated with chiral molecules, its successful realization in solid-state materials, opened a perspective for applications in devices based on the robust properties protected by crystal symmetries. Moreover, materials studies enhance the prospects of providing a satisfactory understanding of CISS, as the origin of the effect in molecules and solids might be similar. The signatures of CISS were found in elemental tellurium and indeed, the simple model helped to attribute the observed effect to the current-induced spin accumulation originating from the radial spin texture.^{15,16} However, the outcomes of the recent experiments suggesting CISS

in CrNb₃S₆, NbSi₂ and TaSi₂,¹⁷⁻¹⁹ which are endowed with more complex electronic structures, were difficult to account for by the models. In addition, these studies revealed the micrometer-range spin relaxation lengths that seemed to be connected with the CISS, but could not be rationalized using simple arguments.

Here, we perform density functional theory (DFT) calculations of the current-induced spin accumulation in Te and TaSi₂, two different chiral materials with strong spin-orbit coupling (SOC). We show that the radial spin texture determined by the chiral point group symmetry gives rise to the unconventional spin accumulation, whereby spins are parallel to the direction of the applied charge current. We also demonstrate that the Weyl-type SOC term locally describing the radial spin texture, may generate a quasi-persistent spin helix in the real space which prevents the spin randomization and results in a very long spin lifetime in a diffusive transport regime. While these arguments support the recent observation of long-range spin signals associated with CISS, the discovery of the unconventional spin accumulation intrinsically protected from the spin decoherence in chiral crystals, will have a far-reaching impact on the design of spintronics devices.

Current-induced spin accumulation for arbitrary SOC. The spin accumulation is a non-equilibrium magnetization induced by an electric current that flows through a non-magnetic material with a large SOC.^{20,21} Even though it was discovered decades ago, experimental studies typically addressed its special case, the Rashba-Edelstein effect present in systems with the Rashba-type spin-momentum locking, such as a two-dimensional electron gas (2DEG), interfaces and surfaces with broken inversion symmetry.²²⁻²⁴ The fact that the spin accumu-

* These three authors contributed equally.

† jagoda.slawska@rug.nl

lation might arise from any other type of SOC, such as Dresselhaus, Weyl, or more complex spin arrangements, was often disregarded and alternative configurations were barely studied, being mostly limited to models.²⁵ In order to establish a link between CISS and the unconventional spin accumulation, quantitative studies of different chiral crystals are required, including those with complex spin textures, where different types of SOC might be simultaneously present in the momentum space.²⁶

Before starting the analysis of specific materials, let us briefly overview the computational approach allowing the calculation of the spin accumulation for arbitrary SOC. The equilibrium electron distribution in a crystal can be described by the Fermi distribution function $f_{\mathbf{k}}^0$. Due to the time reversal symmetry, the expectation values of the spin operator \mathbf{S} at the opposite momenta cancel, resulting in a zero net spin polarization. When an electric field \mathbf{E} is applied, the spin polarized Fermi surface shifts as a result of the applied field and the non-equilibrium distribution $f_{\mathbf{k}} = f_{\mathbf{k}}^0 + \delta f_{\mathbf{k}}$ generates a net spin polarization:

$$\delta \mathbf{s} = \sum_{\mathbf{k}} \langle \mathbf{S} \rangle_{\mathbf{k}} \delta f_{\mathbf{k}} \quad (1)$$

We can calculate $\delta f_{\mathbf{k}}$ in the framework of the semi-classical Boltzmann transport theory and write:

$$\delta \mathbf{s} = \sum_{\mathbf{k}} \langle \mathbf{S} \rangle_{\mathbf{k}} \tau_{\mathbf{k}} (\mathbf{v}_{\mathbf{k}} \cdot \mathbf{E}) \frac{\partial f_{\mathbf{k}}}{\partial E_{\mathbf{k}}} \quad (2)$$

where $\tau_{\mathbf{k}}$ is the relaxation time and $\mathbf{v}_{\mathbf{k}}$ the group velocity. Because the charge current density can be expressed using the same $\delta f_{\mathbf{k}}$,²⁷

$$\mathbf{j}_c = -\frac{e}{V} \sum_{\mathbf{k}} \mathbf{v}_{\mathbf{k}} \delta f_{\mathbf{k}}. \quad (3)$$

we can introduce the spin accumulation tensor χ defined as the ratio of the quantities from Eqs. (2) and (3),

$$\chi^{ji} = -\frac{\sum_{\mathbf{k}} \langle \mathbf{S} \rangle_{\mathbf{k}}^j \mathbf{v}_{\mathbf{k}}^i \frac{\partial f_{\mathbf{k}}}{\partial E_{\mathbf{k}}}}{e \sum_{\mathbf{k}} (\mathbf{v}_{\mathbf{k}}^i)^2 \frac{\partial f_{\mathbf{k}}}{\partial E_{\mathbf{k}}}} \quad (4)$$

in which we assumed the constant relaxation time approximation. The induced spin accumulation per unit volume can be then calculated from the formula,

$$\delta s^j = \chi^{ji} j_i^A \quad (5)$$

where j_i^A is the value of the charge current applied along an arbitrary i direction. Consequently, we can calculate the induced magnetization per unit cell as,

$$\mathbf{m} = -g_s \mu_B V \delta \mathbf{s} / \hbar \quad (6)$$

where $g_s = 2$ is the Landé g-factor, μ_B is Bohr magneton and V denotes the volume of the unit cell.

The quantities required to compute the tensor χ for any material can be evaluated using accurate *ab initio* tight-binding (TB) Hamiltonians constructed from self-consistent quantum-mechanical wavefunctions projected onto a set of atomic orbitals, as detailed in Methods.²⁸

Mechanism of CISS in elemental Te. One of the simplest chiral crystals is trigonal tellurium that crystallizes in two enantiomorphic structures sharing the point group D_3 , right-handed described by the space group $P3_121$ (SG 152) and left-handed belonging to the space group $P3_221$ (SG 154); the structure of the latter is schematically shown in Fig. 1a. Te atoms form covalently bonded spiral chains which are arranged hexagonally and interact with each other via weak van der Waals forces. The three-fold screw symmetry C_3 that determines the chirality runs along the c axis, while additional twofold rotational symmetry axes C_2 lie within the $a - b$ plane. The calculated electronic structure is presented in Fig. 1b-c and agrees well with the earlier theoretical and experimental findings.²⁹⁻³⁴ While it is difficult to reproduce the semiconducting behavior of Te by standard simulations based on the generalized-gradient or local-density approximation, the calculations within the novel pseudo-functional approach ACBN0 yield a gap of 279 meV which is close to the measured value of 330 meV,³⁵ and capture the characteristic 'camelback' shape of the topmost valence band (VB) with a local maximum along the $H - K$ line.³⁶

The strong spin-orbit interaction in Te combined with the lack of the inversion symmetry results in a large spin-splitting of the bands in the whole energy range, but only the topmost VB contributes to electronic and spin transport. Due to the intrinsic p -type doping coming from the vacancies, the Fermi level is shifted by few tens meV below the VBM and the Fermi surface consists of two small pockets around the H and H' points (Fig. 1d), with size and shape depending on the doping. The constant energy contours shown in Fig. 2a correspond to pockets of different sizes projected onto the $k_x - k_z$ plane passing through the H point, while the superimposed color maps represent S_x , S_y , and S_z components of the spin texture.

The peculiar orientation of spins, radial toward the H and H' points is enforced by the three-fold screw symmetry along the $K - H$ line and the twofold symmetry with respect to the $H - H'$ lines in the absence of any mirror planes.^{15,33} Such a spin arrangement, resembling a magnetic monopole in the reciprocal space, is a signature of the prototypical Weyl-type SOC, and may occur only in the systems lacking the mirror symmetry. Moreover, the S_z component prevailing over S_x and S_y , indicates that the spin texture is almost entirely aligned with the k_z , and suggests its quasi-persistent character. The radial spin texture of trigonal Te, including spin polarization nearly parallel to the long direction of the hole pocket, was confirmed by the recent spin- and angle-resolved photoemission spectroscopy (S-ARPES) measurements.^{37,38}

Based on the accurate spin-resolved electronic structure, we calculated the spin accumulation induced by an applied electric current which might be the origin of

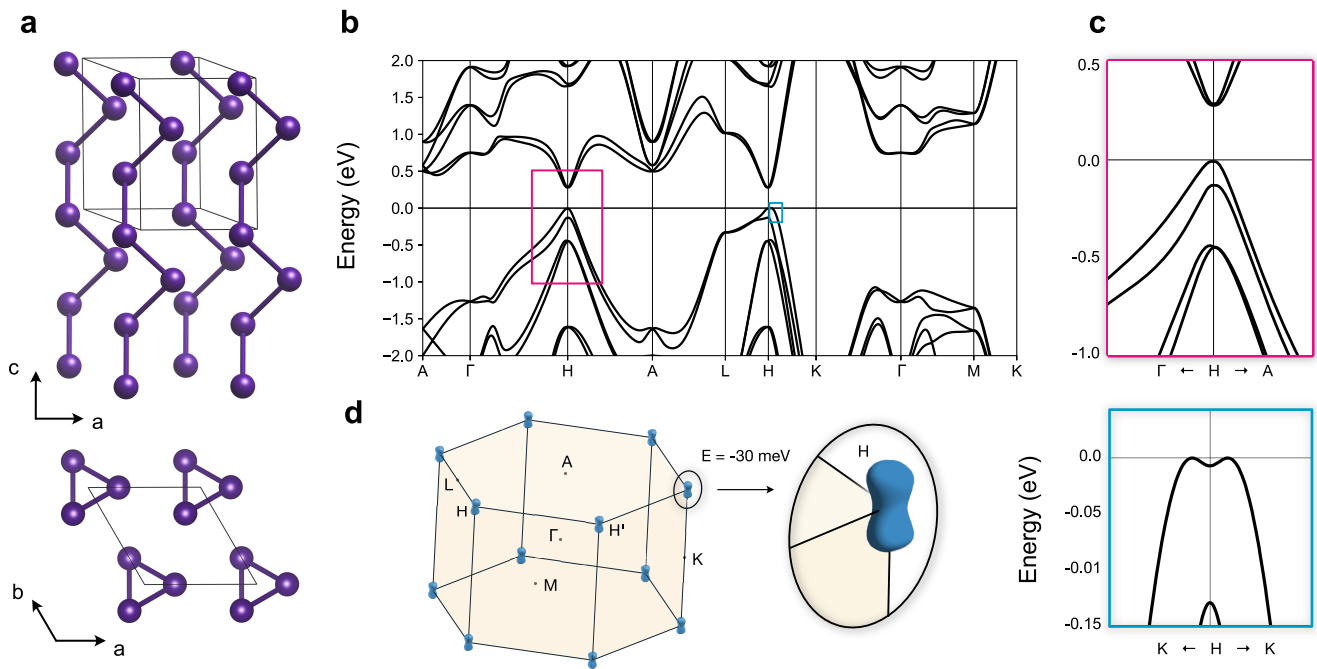


FIG. 1. Crystal structure and electronic properties of chiral tellurium. (a) Side and top view of the left-handed Te (SG 154). (b) Band structure calculated along the high-symmetry lines in the Brillouin zone (BZ), identical for both enantiomers. (c) Zoom on the two regions marked by the color rectangles in (b). The upper panel shows the set of $5p$ lone-pair bands around the H point. The bottom panel illustrates the details of the topmost valence band. (d) Brillouin zone with the high-symmetry points and Fermi surface at $E = -30$ meV; the inset shows a zoom-in of the dumbbell-shaped hole pocket at the H -point.

CISS. Because the spins around the H and H' points are parallel to the momentum, any projection of $\delta\mathbf{s}$ can be achieved as long as the charge current flows in the same direction. We plotted the components δs_z , δs_x and δs_y induced by the electric current of 100 A/cm² along the z , x and y directions, respectively, in the left, middle, and right panel of Fig 2b. Although the spin accumulation perpendicular to the screw axis was never reported in the context of CISS, it is evident that the components δs_x and δs_y , albeit lower than δs_z by an order of magnitude, are present and could be observed in experiments.

The dependence of δs_z on chemical potential (Fig. 2b), closely reflects the electronic structure and the spin texture of the topmost VB. The highest (negative) value of the spin accumulation coincides with the local band minimum at the H point (-8 meV, bottom panel in Fig. 1c), and it decreases when approaching the next valence band with the opposite spin polarization. Although reaching its edge at -130 meV with respect to E_F would require unrealistic values of doping (approximately 2.3×10^{19} vs. $10^{14} - 10^{17}$ cm⁻³ typically observed in Te samples^{39,40}), the decrease in the magnitude can be noticed already above this value. Thus, the low concentrations of holes seem to maximize the spin accumulation in Te. Another factor that may play a relevant role is the temperature (see Fig. 2b). In particular, δs_z tends to drop by a factor of two at room temperature, which cannot be easily explained and requires further systematic studies. In

contrast, the components δs_x and δs_y do not strongly depend neither on doping nor temperature.

Finally, we will compare the current-induced magnetization calculated from the Eq. (6) and displayed in Fig. 2c with the values obtained based on the nuclear magnetic resonance measurements.¹⁵ Our predicted magnetization $10^{-9} \mu_B$ per unit cell agrees well with the model conceived by Furukawa *et al.*,¹⁵ but it is one order of magnitude lower than the value estimated from their experimental data ($10^{-8} \mu_B$). It is still a sufficient agreement to favor the current-induced spin accumulation as the origin of CISS. Importantly, being directly linked to the spin texture, it yields exactly opposite signs of $\delta\mathbf{m}$ for different enantiomers which are connected by the inversion symmetry operation (see Fig. 2c). An alternative mechanism of conversion between charge and spin currents, the spin Hall effect (SHE) does not have such a property. Even though the symmetry of Te (SG 150 or SG 154) allows the unconventional configuration of SHE, whereby charge and spin current as well as the spin polarization of the latter are aligned along the z axis,⁴¹ the left- and right-handed bulk crystals would yield the spin current of the same sign. We note that reversal of the spin Hall conductivity was shown in the ferroelectric GeTe, whose ground states are also related via the inversion symmetry, but it was due to the surface effects in the thin film.⁴² In contrast, the samples of Te had a macroscopic thickness of a few millimeters,¹⁵ thus the

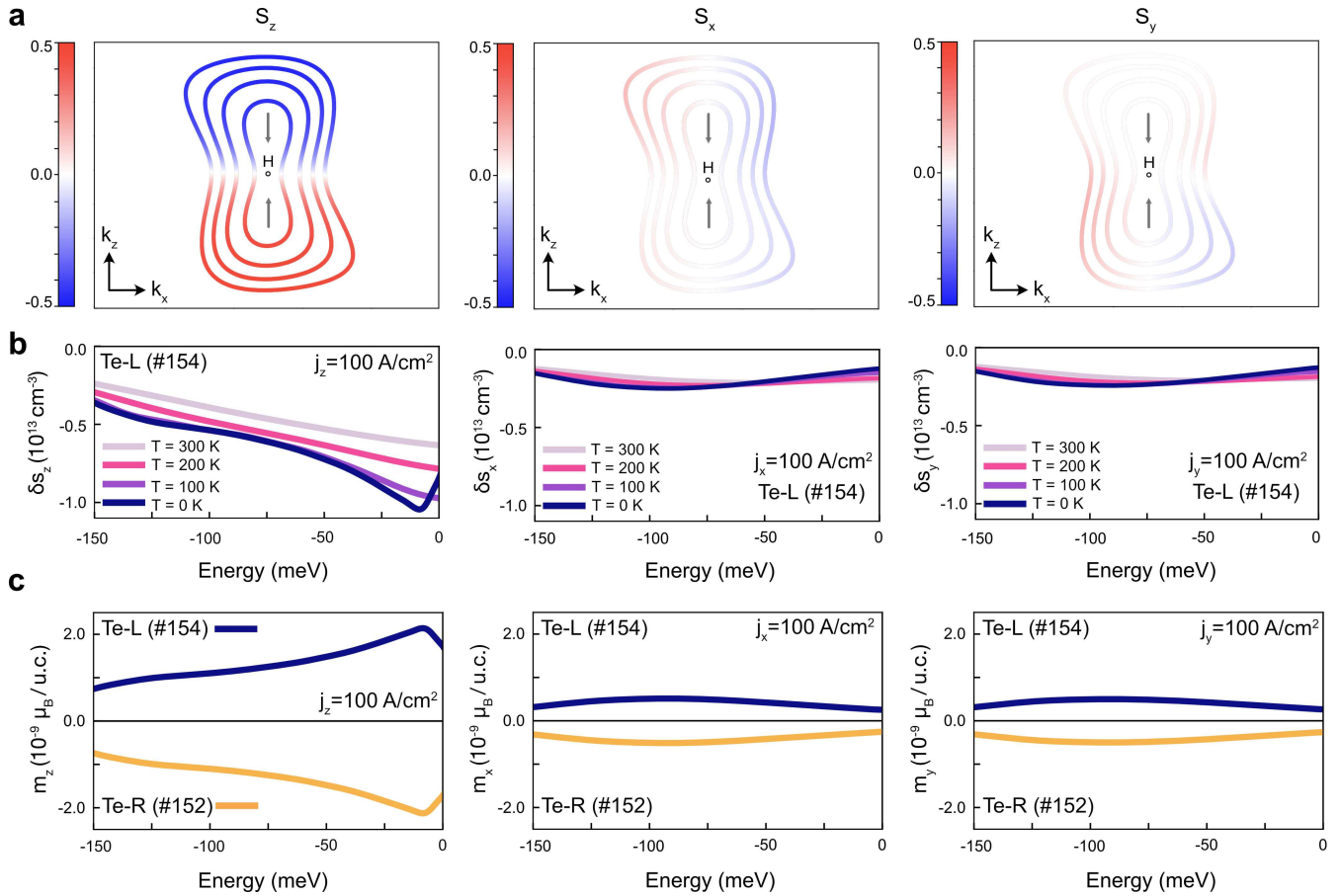


FIG. 2. Spin-resolved electronic structure and spin accumulation in bulk Te. (a) The calculated isoenergy contours projected onto the $k_x - k_z$ plane passing through the H point in the left-handed Te. The energy eigenvalues are selected at 10 meV, 30 meV, 50 meV, and 70 meV below the Fermi level, counting from the center. The color maps superimposed on the contours represent the expectation values of S_x , S_y and S_z shown at the left, middle and right panel, respectively. The spin texture is radial with respect to the H point and nearly persistent along k_z , as indicated by the arrows. (b) Spin accumulation per volume induced by the charge current $j = 100 \text{ A/cm}^2$ applied along z , x and y direction in the left-handed Te, represented by left, middle, and right panel, respectively. Different lines correspond to temperatures in the range from 0 K to 300 K. (c) The corresponding magnetization per unit cell calculated for the left-handed (blue lines) and right-handed Te (orange lines) at 0 K.

surface/interface SHE must be excluded in this case.

CISS in a semimetallic disilicide TaSi₂. Inspired by the spin transport experiments that revealed signatures of the CISS response in the chiral disilicides, we performed the calculations for chiral TaSi₂.¹⁹ Its right-handed structure belongs to the space group P6₂22 (SG 180) and the left-handed one is characterized by the space group P6₄22 (SG 181); both enantiomers are displayed in Fig. 3a-b. The hexagonal unit cell contains two pairs of intertwined Ta-Si-Ta chains with different helicity running along the c direction, which is reversed for the opposite enantiomers. The left-handed and right-handed structures are distinguished by the sixfold screw symmetry C_6 along the c -axis, while the additional C_2 rotational symmetries are defined with respect to the crystal $a - b$ face diagonals (see Fig. 3c). The calculated electronic structure shown in Fig. 3d is in a good agreement with the existing theoretical and experimental reports.⁴⁴⁻⁴⁶

TaSi₂ is a Weyl semimetal and indeed, the energy dispersion contains several degenerate crossings protected by the nonsymmorphic symmetry, for example the nodes at the M and H points that lie close to the Fermi level. The shape of the Fermi surface (Fig. 3e), consisting of four non-intersecting sheets is also in line with the results of the previous de Haas-van Alphen experiments.⁴⁴

The current-induced spin accumulation in the semimetallic TaSi₂ is governed by the spin texture of the Fermi surface. Because it contains multiple nested sheets with different spin patterns, it is not straightforward to analyze the full landscape of the spin-orbit field inside the BZ. Nevertheless, the linear-in- k spin arrangement at the high-symmetry points can be predicted with the help of the group theory and further verified by the DFT calculations. Following the study by Mera Acosta *et al.*,²⁶ we note that the crystallographic point group D_6 describing TaSi₂ may yield the purely radial Weyl

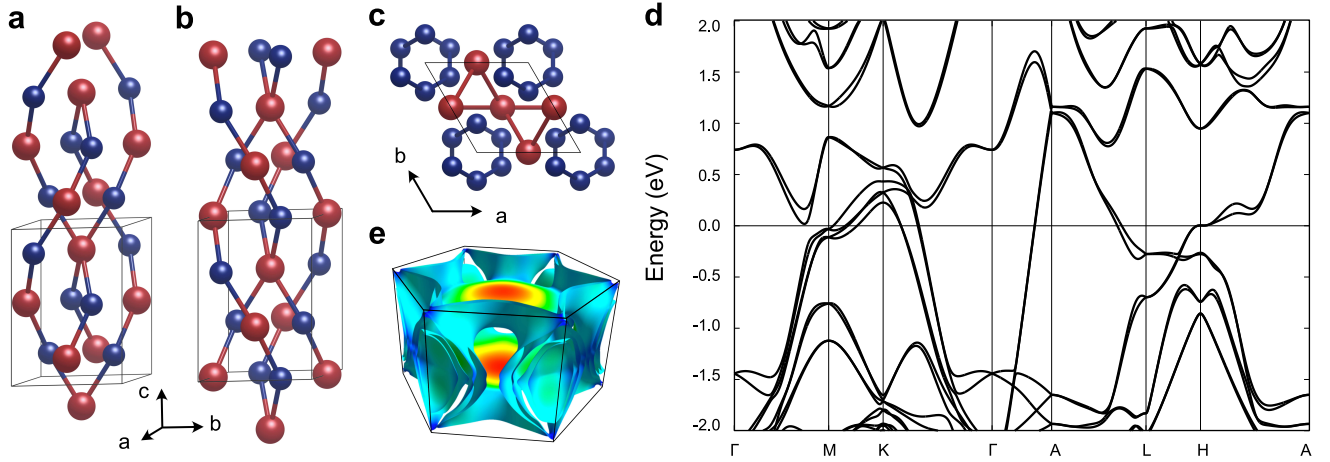


FIG. 3. Structure and electronic properties of chiral TaSi₂. (a) Side view of the right-handed TaSi₂ (SG 180). Ta atoms are denoted as red and Si atoms as blue balls. (b) Top and side view of the left-handed TaSi₂ (SG 181). (c) The calculated Fermi surface ($E = E_F$) consisting of four nested sheets. The color scheme reflects the Fermi velocity.⁴³ (d) Band structure calculated along the high-symmetry lines in the momentum space. The high-symmetry points are consistent with the labels in Fig. 1.

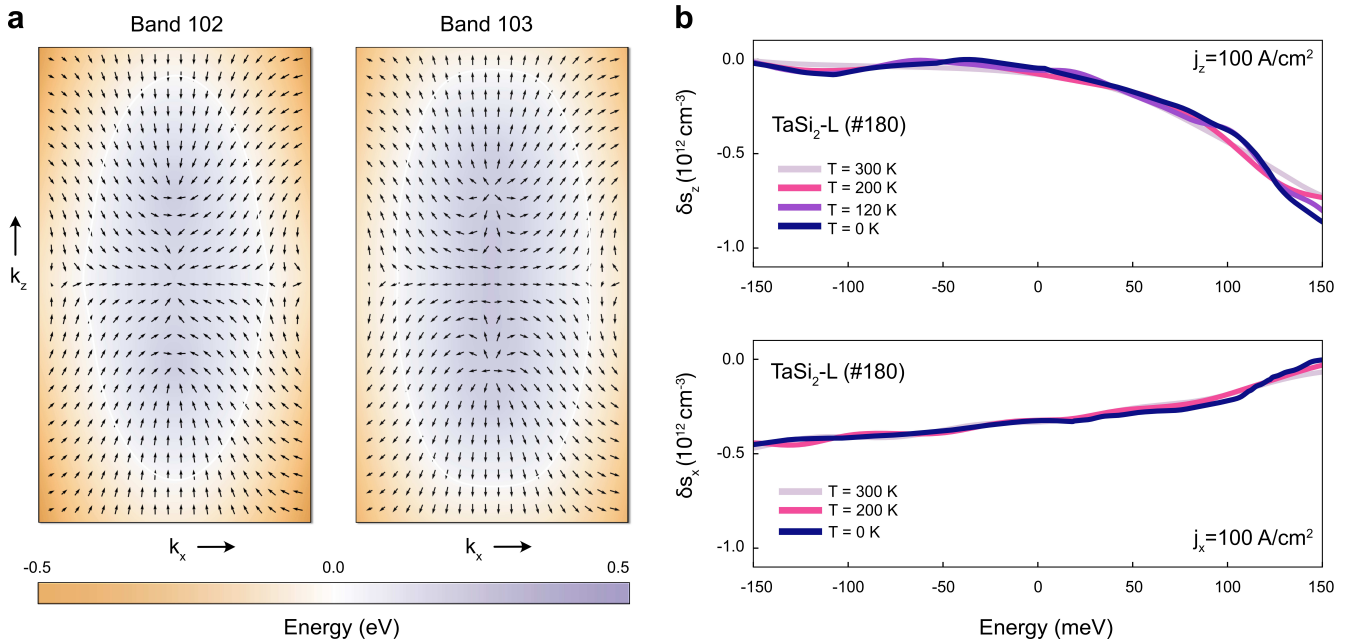


FIG. 4. Spin texture and spin accumulation in the right-handed TaSi₂ (SG 180). (a) Energy eigenvalues and spin texture of the two innermost band visible in Fig. 3e projected on the $k_x - k_z$ plane passing through the K point; the K point is located exactly at the center. The S_y components are included only in the norms of the spin vectors. The multiple arrows serve for a better illustration of the trend, but only those coinciding with the Fermi contour – denoted as the white line – contribute to the spin accumulation. (b) The calculated spin accumulation vs energy; the components δs_z and δs_x are shown in the upper and bottom panel, respectively. The omitted δs_y is similar to δs_x . The colors of the lines correspond to different temperatures.

spin texture at the k -vectors possessing the point group symmetry D_3 or D_6 . Using the Bilbao Crystallographic Server,^{47,48} we determined little point groups of all the high-symmetry points (Γ , A , K , H and M) and we found that most of them can be the ‘source’ or ‘sink’ of the ra-

dial spin texture. Only the M point described by the little point group D_2 allows both Weyl and Dresselhaus spin arrangement.²⁶ As an example, Fig. 4a illustrates the spin texture of the two innermost bands contributing to the Fermi surface, projected onto the $k_x - k_z$ plane

around the K point. The spin textures are almost perfectly radial with a visible persistent component S_z that seems to be enforced by the elongated band shapes. In a 3D k -space, these FS would resemble ellipsoids, one inside another, with the hedgehog-like spin textures.

The radial spin arrangements dominating in the BZ, generate the unconventional spin accumulation that may manifest as CISS in TaSi₂. The calculated δs induced by the electric current of 100 A/cm² flowing in the directions parallel and perpendicular to the screw axis is shown in Fig. 4b. The results are presented as the energy dependence to better show the connection with the band structure, but TaSi₂ is semimetallic and mostly the values close to the Fermi level are relevant for the transport. Surprisingly, δs_z at E_F is nearly two orders of magnitude lower than in the slightly doped Te ($10^{11}/\text{cm}^3$ vs $10^{13}/\text{cm}^3$), while δs_x is lower by one order of magnitude. Such a difference seems to be due to the fact that two pairs of bands with the opposite polarization simultaneously cross the Fermi level. This contrasts with the case of Te which FS consists of the two identical spin-polarized pockets. In fact, the increase of the δs_z magnitude above E_F in TaSi₂ can be assigned to the emergence of an isolated strongly spin-polarized pocket at +20 meV.

CISS response in the chiral disilicides was suggested based on the spin transport experiments for left- and right-handed NbSi₂ and TaSi₂.¹⁹ Although these reports were quantitative and cannot be compared with the result of the DFT calculations, we believe that the current-induced spin accumulation may give rise to the observed interconversion between charge and spin current. First, we note that the unconventional SHE in TaSi₂ (SG 180) is forbidden by the symmetry and could not contribute to the spin transport.⁴¹ Second, the quasi-persistent character of the spin texture enforced by the crystal symmetry (Fig. 4a) indicates that the spins should be partially protected from scattering, and capable to diffuse to the detection electrode. Below, we will explicitly show that the anti-symmetric SOC arising from the monoaxial screw symmetry, and approximated by the linear-in- k Weyl term in the Hamiltonian,^{26,49} generates the *near persistent spin helix* in the real space and gives rise to a potentially infinite spin lifetime in chiral materials.

Spin transport over macroscopic distances. To understand the emergence of the *persistent spin helix*, let us consider the free electron dispersion $H_0 = \hbar^2 \mathbf{k}^2 / 2m$ where m is the effective electron mass and $\mathbf{k} = (k_x, k_y, k_z)$. We also consider the Weyl spin-orbit coupling term $H_{so} = \alpha_x k_x \hat{\sigma}_x + \alpha_y k_y \hat{\sigma}_y + \alpha_z k_z \hat{\sigma}_z$, where $\hat{\sigma}_i$ denotes the Pauli spin matrices and α_i are the SOC parameters along $i = x, y, z$ directions. Our first principles calculations show that the spin textures of Te and TaSi₂ are strongly enhanced along the direction of the screw axis, as illustrated in Fig. 2a and Fig. 4a. More specifically, in the case of Te the SOC parameters are $\alpha_z \gg \alpha_j$ for $j = x, y$, whereas in TaSi₂ we have $\alpha_z > \alpha_x > \alpha_y$.

The Hamiltonian is then, without the loss of generality,

$$H = H_0 + H_{so} \simeq \frac{\hbar^2 \mathbf{k}_{\parallel}^2}{2m} + \frac{\hbar^2 k_z^2}{2m} + \alpha_z k_z \hat{\sigma}_z, \quad (7)$$

where $\mathbf{k}_{\parallel}^2 = k_x^2 + k_y^2$. The Hamiltonian is diagonal in the spin space and its eigenvalues are

$$E_{\uparrow, \downarrow}(\mathbf{k}) = \frac{\hbar^2 \mathbf{k}_{\parallel}^2}{2m} + \frac{\hbar^2}{2m} \left(k_z \mp \frac{m\alpha_z}{\hbar^2} \right)^2 - \frac{\hbar^2}{2m} \left(\frac{m\alpha_z}{\hbar^2} \right)^2, \quad (8)$$

where $E_{\uparrow, \downarrow}$ denote bands with \uparrow, \downarrow spin projections, respectively. The Eq.(8) satisfies the shifting property

$$E_{\uparrow}(\mathbf{k}) = E_{\downarrow}(\mathbf{k} + \mathbf{Q}), \quad (9)$$

proposed by Berenevig *et al.*, which implies that the Fermi surfaces consists of two circles, shifted by magic-shifting vector $\mathbf{Q} = 2m\alpha_z/\hbar^2$.⁵⁰ Following the analysis similar to the one for the Rashba-Dresselhaus model with equal SOC parameters,⁵⁰ we identify the existence of the $SU(2)$ symmetry of the Hamiltonian in Eq.(7), which is robust against disorder and Coulomb interaction and can give rise to, ideally, infinite spin lifetime along the z -direction (see Fig. 5). The presence of the weak SOC along the x and y directions, perturbs the exact $SU(2)$ symmetry. The emergence of the *near persistent spin helix* explains the finite, but sizable spin relaxation length suggested in the chiral crystals,^{17,19} conceiving a more complete picture of the possible CISS response.

In summary, we calculated the spin accumulation that originates from the radial spin texture of chiral materials, using for the first time the accurate DFT-based approach. By analyzing two different materials, Te and TaSi₂, studied experimentally in the context of CISS, we showed that the current-induced spin accumulation is the plausible explanation of its mechanism. The reversal of sign associated with different chiralities is naturally ensured by the fact that the left- and right-handed crystals are related through the inversion symmetry operation, which yields exactly opposite spin polarization of all the bands in the two enantiomers. We also proved via the analysis of the calculated spin textures and a general Weyl Hamiltonian, that the chiral materials can host the quasi-persistent spin helix that emerges in the real space as a consequence of the crystal symmetry. It protects spins against scattering and ensures a sizable spin relaxation length, which seems to be in line with the recent observation of micrometer-range spin transport associated with CISS. The possibility of electric generation of spin accumulation intrinsically linked to the long spin lifetime will have important implications for spintronics devices.

Our results open exciting perspectives for more advanced first principles calculations. Although the occurrence of the prototypical Weyl spin texture in the high-symmetry points in the momentum space can be deduced from the group theory, the overall landscape of the spin-orbit field in the BZ is more difficult to predict. Besides, the contribution of a particular spin polarized

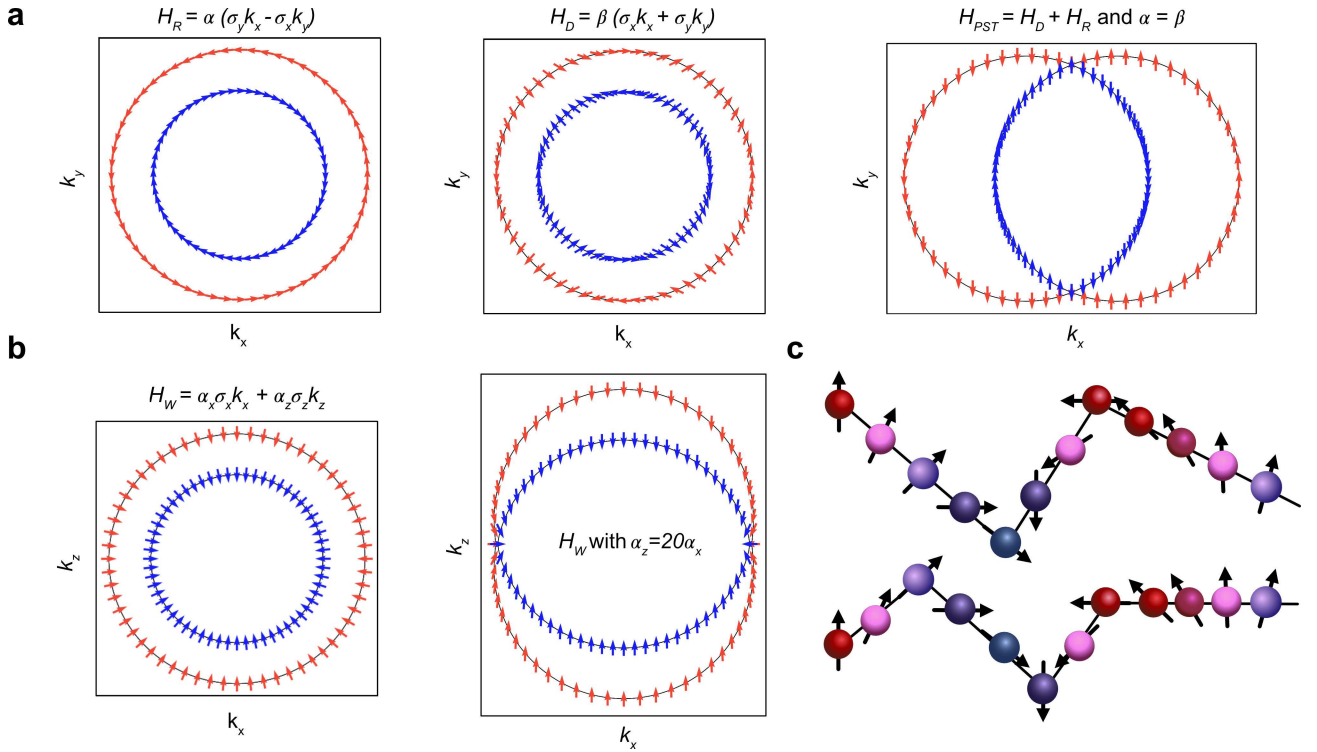


FIG. 5. Persistent spin texture and spin helix in the Rashba-Dresselhaus (RD) and Weyl (W) models enhancing spin transport in systems with strong SOC. (a) Pure Rashba (left) and Dresselhaus (middle) models; their combination with $\alpha = \beta$ (right) generates a persistent spin texture in the momentum space. (b) Analogous mechanism contributing to a persistent spin texture in the Weyl model describing the radial spin texture; Weyl Hamiltonian with equal ($\alpha_z = \alpha_x$) parameters (left) and with the prevailing $\alpha_z \sigma_z$ term (right). The latter, with $\alpha_z = 20\alpha_x$ closely resembles the spin texture of Te (see Fig. 2a). (c) Schematic illustration of a persistent spin helix in the real space observed in quantum wells with balanced Rashba and Dresselhaus terms.⁵¹ The collective spin is a conserved quantity due to the emergence of the $SU(2)$ symmetry. The quasi-persistent spin texture described by the Weyl Hamiltonian will lead to a similar effect protecting the spin transport in CISS.

band to spin accumulation will depend on the exact electronic structure of the specific material. Therefore, a high-throughput search can be required to find the most promising materials belonging to one of the 65 Sohncke space groups.⁴⁹ A further step toward the complete understanding of CISS in general systems is to study the role of the electron-electron and electron-phonon interaction, especially in connection with the weak SOC, which remains within the reach of our computational approach.

METHODS

We performed calculations based on the density functional theory (DFT) using the QUANTUM ESPRESSO package.^{52,53} We treated the ion-electron interaction with the fully relativistic pseudopotentials from the pslibrary (0.2) database,⁵⁴ and expanded the electron wave functions in a plane wave basis set with the cutoff of 80 Ry. The exchange and correlation interaction was taken into account within the generalized gradient approximation (GGA) parameterized by the Perdew, Burke, and Ernzerhof (PBE) functional.⁵⁵ The Te crystals were modeled

using hexagonal unit cells containing three atoms, which were fully optimized with the convergence criteria for energy and forces set to 10^{-5} Ry and 10^{-4} Ry/bohr, respectively. We applied the Hubbard correction calculated self-consistently using the ACBN0 method,⁵⁶ which value $U_{5p} = 3.81$ eV was included in the relaxations and the electronic structure calculations. The lattice constants were optimized to $a = b = 4.51$ Å and $c = 5.86$ Å. TaSi₂ was modeled in a hexagonal unit cell containing nine atoms. The lattice parameters were fixed to the experimental values $a = b = 4.78$ Å and $c = 6.57$ Å,⁴⁵ while the internal coordinates were relaxed. The BZ integrations were performed using the Monkhorst-Pack scheme with k -points grids of $22 \times 22 \times 16$ and $16 \times 16 \times 12$ for Te and TaSi₂, respectively. The Gaussian smearing of 0.001 Ry was chosen as the orbital occupation scheme. SOC was included self-consistently in all the calculations.

Current-induced spin accumulation was evaluated as a post-processing step using the tight-binding (TB) approach implemented in the PAOFLOW code.^{57,58} We have started with the *ab initio* wavefunctions, projecting them onto the pseudoatomic orbitals in order to construct accurate tight-binding (PAO) Hamiltonians.^{59,60}

We further interpolated these Hamiltonians onto ultra-dense k -points meshes of $140 \times 140 \times 110$ for Te and $80 \times 80 \times 60$ for TaSi₂, and we directly evaluated the quantities that are required to compute spin accumulation from Eq.(4). In particular, the group velocities $\mathbf{v}_{\mathbf{k}}$ are calculated as Hamiltonian's gradients $(1/\hbar)dH/d\mathbf{k}$, and the spin polarization of each eigenstate $\psi(\mathbf{k})$ is automatically taken as the expectation value of the spin operator $\langle \psi(\mathbf{k}) | \mathbf{S} | \psi(\mathbf{k}) \rangle$.⁵⁸ For an arbitrary energy E , the derivative of the Fermi distribution at zero temperature is equal to $\delta(E_{\mathbf{k}} - E)$ which we approximated with a Gaussian function. For $T > 0$, we explicitly calculated the derivative of the Fermi-Dirac distribution. We note that the adaptive smearing method could not be applied in this case, and a larger k -grid of $140 \times 140 \times 100$ had to be used to converge the calculation of TaSi₂ (Fig. 4c). The influence of the temperature on the electronic structures was not taken into account.

ACKNOWLEDGMENTS

We are grateful to Xu Yang and Caspar van der Wal for the interesting discussions that inspired us to initiate this project and to Bart van Wees for the insightful remarks on the manuscript. J.S. acknowledges the Rosalind Franklin Fellowship from the University of Groningen. The calculations were carried out on the Dutch national e-infrastructure with the support of SURF Cooperative (EINF-2070), on the Peregrine high performance computing cluster of the University of Groningen and in the Texas Advanced Computing Center at the University of Texas, Austin.

AUTHOR CONTRIBUTION

J.S., A.R. and K.T performed the DFT calculations. A.R. conceived and analyzed model Hamiltonians. J.S, F.C. and M.B.N supported by A.R. and A.J. implemented the method. A.R. and J.S. compiled the figures and wrote the manuscript. J.S. proposed and supervised the project. All authors contributed to the analysis and discussion of the results.

-
- [1] E. Hendry, T. Carpy, J. Johnston, M. Popland, R. V. Mikhaylovskiy, A. J. Lapthorn, S. M. Kelly, L. D. Barron, N. Gadegaard, and M. Kadodwala, Ultrasensitive detection and characterization of biomolecules using superchiral fields, *Nature Nanotechnology* **5**, 783 (2010).
- [2] C. Kelly, D. A. MacLaren, K. McKay, A. McFarlane, A. S. Karimullah, N. Gadegaard, L. D. Barron, S. Franke-Arnold, F. Crimin, J. B. Götze, S. M. Barnett, and M. Kadodwala, Controlling the symmetry of inorganic ionic nanofilms with optical chirality, *Nature Communications* **11**, 5169 (2020).
- [3] M. Hentschel, M. Schäferling, X. Duan, H. Giessen, and N. Liu, Chiral plasmonics, *Science Advances* **3**, e1602735 (2017).
- [4] D. Ayuso, O. Neufeld, A. F. Ordonez, P. Declewa, G. Lerner, O. Cohen, M. Ivanov, and O. Smirnova, Synthetic chiral light for efficient control of chiral light-matter interaction, *Nature Photonics* **13**, 866 (2019).
- [5] R. Naaman, Y. Paltiel, and D. H. Waldeck, Chiral molecules and the electron spin, *Nature Reviews Chemistry* **3**, 250 (2019).
- [6] D. H. Waldeck, R. Naaman, and Y. Paltiel, The spin selectivity effect in chiral materials, *APL Materials* **9**, 040902 (2021).
- [7] F. Evers, A. Aharony, N. Bar-Gill, O. Entin-Wohlman, P. Hedegård, O. Hod, P. Jelinek, G. Kamieniarz, M. Lemeshko, K. Michaeli, V. Mujica, R. Naaman, Y. Paltiel, S. Refaely-Abramson, O. Tal, J. Thijssen, M. Thoss, J. M. van Ruitenbeek, L. Venkataraman, D. H. Waldeck, B. Yan, and L. Kronik, Theory of chirality induced spin selectivity: Progress and challenges, *Advanced Materials* **n/a**, 2106629.
- [8] T. S. Metzger, S. Mishra, B. P. Bloom, N. Goren, A. Neubauer, G. Shmul, J. Wei, S. Yochelis, F. Tassinari, C. Fontanesi, D. H. Waldeck, Y. Paltiel, and R. Naaman, The electron spin as a chiral reagent, *Angewandte Chemie* **59**, 1670 (2020).
- [9] A. Kumar, E. Capua, M. K. Kesharwani, J. M. L. Martin, E. Sitbon, D. H. Waldeck, and R. Naaman, Chirality-induced spin polarization places symmetry constraints on biomolecular interactions, *Proceedings of the National Academy of Sciences* **114**, 2474 (2017).
- [10] S.-H. Yang, Spintronics on chiral objects, *Applied Physics Letters* **116**, 120502 (2020).
- [11] S.-H. Yang, R. Naaman, Y. Paltiel, and S. S. P. Parkin, Chiral spintronics, *Nature Reviews Physics* **3**, 328 (2021).
- [12] X. Yang, C. H. van der Wal, and B. J. van Wees, Detecting chirality in two-terminal electronic nanodevices, *Nano Letters* **20**, 6148 (2020).
- [13] M. Suda, Y. Thathong, V. Promarak, H. Kojima, M. Nakamura, T. Shiraogawa, M. Ehara, and H. M. Yamamoto, Light-driven molecular switch for reconfigurable spin filters, *Nature Communications* **10**, 2455 (2019).
- [14] G. Koplovitz, D. Primc, O. B. Dor, S. Yochelis, D. Rotem, D. Porath, and Y. Paltiel, Magnetic nanoplatelet-based spin memory device operating at ambient temperatures, *Advanced Materials* **29**, 1606748 (2017).
- [15] T. Furukawa, Y. Shimokawa, K. Kobayashi, and T. Itou, Observation of current-induced bulk magnetization in elemental tellurium, *Nature Communications* **8**, 954 (2017).
- [16] T. Furukawa, Y. Watanabe, N. Ogasawara, K. Kobayashi, and T. Itou, Current-induced mag-

- netization caused by crystal chirality in nonmagnetic elemental tellurium, *Physical Review Research* **3**, 023111 (2021).
- [17] A. Inui, R. Aoki, Y. Nishiue, K. Shiota, Y. Kousaka, H. Shishido, D. Hirobe, M. Suda, J.-i. Ohe, J.-i. Kishine, H. M. Yamamoto, and Y. Togawa, Chirality-induced spin-polarized state of a chiral crystal CrNb_3S_6 , *Physical Review Letters* **124**, 166602 (2020).
- [18] Y. Nabei, D. Hirobe, Y. Shimamoto, K. Shiota, A. Inui, Y. Kousaka, Y. Togawa, and H. M. Yamamoto, Current-induced bulk magnetization of a chiral crystal CrNb_3S_6 , *Applied Physics Letters* **117**, 052408 (2020).
- [19] K. Shiota, A. Inui, Y. Hosaka, R. Amano, Y. Ōnuki, M. Hedo, T. Nakama, D. Hirobe, J.-i. Ohe, J.-i. Kishine, H. M. Yamamoto, H. Shishido, and Y. Togawa, Chirality-induced spin polarization over macroscopic distances in chiral disilicide crystals, *Physical Review Letters* **127**, 126602 (2021).
- [20] A. G. Aronov and Y. B. Lyanda-Geller, Nuclear electric resonance and orientation of carrier spins by an electric field, *Soviet Journal of Experimental and Theoretical Physics Letters* **50**, 431 (1989).
- [21] A. Aronov, Y. B. Lyanda-Geller, G. E. Pikus, and D. Parsons, Spin polarization of electrons by an electric current, *Soviet Journal of Experimental and Theoretical Physics* **73**, 537 (1991).
- [22] A. Johansson, B. Gobel, J. Henk, M. Bibes, and I. Mertig, Spin and orbital Edelstein effects in a two-dimensional electron gas: Theory and application to SrTiO_3 interfaces, *Physical Review Research* **3**, 013275 (2021).
- [23] A. Johansson, J. Henk, and I. Mertig, Theoretical aspects of the Edelstein effect for anisotropic two-dimensional electron gas and topological insulators, *Physical Review B* **93**, 195440 (2016).
- [24] T. S. Ghiasi, A. A. Kaverzin, P. J. Blah, and B. J. van Wees, Charge-to-spin conversion by the Rashba–Edelstein effect in two-dimensional van der Waals heterostructures up to room temperature, *Nano Letters* **19**, 5959 (2019).
- [25] L. Tao and E. Y. Tsymlal, Spin-orbit dependence of anisotropic current-induced spin polarization, *Physical Review B* **104**, 085438 (2021).
- [26] C. M. Acosta, L. Yuan, G. M. Dalpian, and A. Zunger, Different shapes of spin textures as a journey through the Brillouin zone, *Physical Review B* **104**, 104408 (2021).
- [27] J. M. Ziman, *Principles of the Theory of Solids* (Cambridge University Press, 1972).
- [28] L. A. Agapito, A. Ferretti, A. Calzolari, S. Curtarolo, and M. Buongiorno Nardelli, Effective and accurate representation of extended Bloch states on finite Hilbert spaces, *Physical Review B* **88**, 165127 (2013).
- [29] T. Doi, K. Nakao, and H. Kamimura, The valence band structure of tellurium. i. the k-p perturbation method, *Journal of the Physical Society of Japan* **28**, 36 (1970).
- [30] V. A. Shalygin, A. N. Sofronov, L. E. Vorob'ev, and I. I. Farbshtein, Current-induced spin polarization of holes in tellurium, *Physics of the Solid State* **54**, 2362 (2012).
- [31] L. A. Agapito, N. Kioussis, W. A. Goddard, and N. P. Ong, Novel family of chiral-based topological insulators: Elemental tellurium under strain, *Physical Review Letters* **110**, 176401 (2013).
- [32] S. S. Tsirkin, P. A. Puente, and I. Souza, Gyrotropic effects in trigonal tellurium studied from first principles, *Physical Review B* **97**, 035158 (2018).
- [33] M. Hirayama, R. Okugawa, S. Ishibashi, S. Murakami, and T. Miyake, Weyl node and spin texture in trigonal tellurium and selenium, *Physical Review Letters* **114**, 206401 (2015).
- [34] K. Nakayama, M. Kuno, K. Yamauchi, S. Souma, K. Sugawara, T. Oguchi, T. Sato, and T. Takahashi, Band splitting and Weyl nodes in trigonal tellurium studied by angle-resolved photoemission spectroscopy and density functional theory, *Physical Review B* **95**, 125204 (2017).
- [35] V. B. Anzin, M. I. Eremets, Y. V. Kosichkin, A. I. Nadezhdinskii, and A. M. Shirokov, Measurement of the energy gap in tellurium under pressure, *Physica Status Solidi (a)* **42**, 385 (1977).
- [36] S. S. Tsirkin, I. Souza, and D. Vanderbilt, Composite Weyl nodes stabilized by screw symmetry with and without time-reversal invariance, *Physical Review B* **96**, 045102 (2017).
- [37] G. Gatti, D. Gosálbez-Martínez, S. S. Tsirkin, M. Fanciulli, M. Puppini, S. Polishchuk, S. Moser, L. Testa, E. Martino, S. Roth, P. Bugnon, L. Moreschini, A. Bostwick, C. Jozwiak, E. Rotenberg, G. Di Santo, L. Petaccia, I. Vobornik, J. Fujii, J. Wong, D. Jariwala, H. A. Atwater, H. M. Rønnow, M. Chergui, O. V. Yazyev, M. Grioni, and A. Crepaldi, Radial spin texture of the Weyl fermions in chiral tellurium, *Physical Review Letters* **125**, 216402 (2020).
- [38] M. Sakano, M. Hirayama, T. Takahashi, S. Akebi, M. Nakayama, K. Kuroda, K. Taguchi, T. Yoshikawa, K. Miyamoto, T. Okuda, K. Ono, H. Kumigashira, T. Ideue, Y. Iwasa, N. Mitsuishi, K. Ishizaka, S. Shin, T. Miyake, S. Murakami, T. Sasagawa, and T. Kondo, Radial spin texture in elemental tellurium with chiral crystal structure, *Physical Review Letters* **124**, 136404 (2020).
- [39] N. Zhang, G. Zhao, L. Li, P. Wang, L. Xie, B. Cheng, H. Li, Z. Lin, C. Xi, J. Ke, M. Yang, J. He, Z. Sun, Z. Wang, Z. Zhang, and C. Zeng, Magnetotransport signatures of Weyl physics and discrete scale invariance in the elemental semiconductor tellurium, *Proceedings of the National Academy of Sciences* **117**, 11337 (2020).
- [40] T. Ideue, M. Hirayama, H. Taiko, T. Takahashi, M. Murase, T. Miyake, S. Murakami, T. Sasagawa, and Y. Iwasa, Pressure-induced topological phase transition in noncentrosymmetric elemental tellurium, *Proceedings of the National Academy of Sciences* **116**, 25530 (2019).
- [41] A. Roy, M. H. Guimarães, and J. Ślawińska, Unconventional spin Hall effects in non-magnetic solids, [arXiv:2110.09242](https://arxiv.org/abs/2110.09242) (2021).
- [42] S. Varotto, L. Nessi, S. Cecchi, J. Ślawińska, P. Noel, S. Petro, F. Fagiani, A. Novati, M. Cantoni, D. Petti, E. Albisetti, M. Costa, R. Calarco, M. Buongiorno Nardelli, M. Bibes, S. Picozzi, J.-P. Attane, L. Vila, R. Bertacco, and C. Rinaldi, Room-temperature ferroelectric switching of spin-to-charge conversion in germanium telluride, *Nature Electronics* **4**, 740 (2021).
- [43] M. Kawamura, FermiSurfer: Fermi-surface viewer providing multiple representation schemes, *Computer Physics Communications* **239**, 197 (2019).
- [44] Y. Ōnuki, A. Nakamura, T. Uejo, A. Teruya, M. Hedo, T. Nakama, F. Honda, and H. Harima, Chiral-structure-driven split fermi surface properties in TaSi_2 , NbSi_2 , and VSi_2 , *Journal of the Physical Society of Japan* **83**, 061018 (2014).

- [45] H. Zhu, T. Yang, Y. Zhou, S. Hua, and J. Yang, Theoretical prediction on the structural, electronic, mechanical, and thermodynamic properties of TaSi₂ with a C₄₀ structure under pressure, *Zeitschrift für Naturforschung A* **74**, 353 (2019).
- [46] C. A. C. Garcia, D. M. Nenno, G. Varnavides, and P. Narang, Anisotropic phonon-mediated electronic transport in chiral Weyl semimetals, *Physical Review Materials* **5**, L091202 (2021).
- [47] M. I. Aroyo, J. M. Perez-Mato, C. Capillas, E. Kroumova, S. Ivantchev, G. Madariaga, A. Kirov, and H. Wondratschek, Bilbao Crystallographic Server: I. Databases and crystallographic computing programs, *Zeitschrift für Kristallographie - Crystalline Materials* **221**, 15 (2006).
- [48] M. I. Aroyo, A. Kirov, C. Capillas, J. M. Perez-Mato, and H. Wondratschek, Bilbao Crystallographic Server: II. Representations of crystallographic point groups and space groups, *Acta Crystallographica Section A* **62**, 115 (2006).
- [49] G. Chang, B. J. Wieder, F. Schindler, D. S. Sanchez, I. Belopolski, S.-M. Huang, B. Singh, D. Wu, T.-R. Chang, T. Neupert, *et al.*, Topological quantum properties of chiral crystals, *Nature Materials* **17**, 978 (2018).
- [50] B. A. Bernevig, J. Orenstein, and S.-C. Zhang, Exact SU(2) symmetry and persistent spin helix in a spin-orbit coupled system, *Physical Review Letters* **97**, 236601 (2006).
- [51] J. D. Koralek, C. P. Weber, J. Orenstein, B. A. Bernevig, S.-C. Zhang, S. Mack, and D. D. Awschalom, Emergence of the persistent spin helix in semiconductor quantum wells, *Nature* **458**, 610 (2009).
- [52] P. Giannozzi, S. Baroni, N. Bonini, M. Calandra, R. Car, C. Cavazzoni, D. Ceresoli, G. L. Chiarotti, M. Cococcioni, I. Dabo, A. D. Corso, S. de Gironcoli, S. Fabris, G. Fratesi, R. Gebauer, U. Gerstmann, C. Gougoussis, A. Kokalj, M. Lazzeri, L. Martin-Samos, N. Marzari, F. Mauri, R. Mazzarello, S. Paolini, A. Pasquarello, L. Paulatto, C. Sbraccia, S. Scandolo, G. Sclauzero, A. P. Seitsonen, A. Smogunov, P. Umari, and R. M. Wentzcovitch, QUANTUM ESPRESSO: a modular and open-source software project for quantum simulations of materials, *Journal of Physics: Condensed Matter* **21**, 395502 (2009).
- [53] P. Giannozzi, O. Andreussi, T. Brumme, O. Bunau, M. Buongiorno Nardelli, M. Calandra, R. Car, C. Cavazzoni, D. Ceresoli, M. Cococcioni, N. Colonna, I. Carnimeo, A. Dal Corso, S. De Gironcoli, P. Delugas, R. A. DiStasio Jr, A. Ferretti, A. Floris, G. Fratesi, G. Fugallo, R. Gebauer, U. Gerstmann, F. Giustino, T. Gorni, J. Jia, M. Kawamura, H.-Y. Ko, A. Kokalj, E. Kucukbenli, M. Lazzeri, M. Marsili, N. Marzari, F. Mauri, N. L. Nguyen, H.-V. Nguyen, A. Otero-de-la Roza, L. Paulatto, S. Ponc e, D. Rocca, R. Sabatini, B. Santra, M. Schlipf, A. P. Seitsonen, A. Smogunov, I. Timrov, T. Thonhauser, P. Umari, N. Vast, X. Wu, and S. Baroni, Advanced capabilities for materials modelling with QUANTUM ESPRESSO, *Journal of Physics: Condensed Matter* **29**, 465901 (2017).
- [54] A. D. Corso, Pseudopotentials periodic table: From H to Pu, *Computational Materials Science* **95**, 337 (2014).
- [55] J. P. Perdew, K. Burke, and M. Ernzerhof, Generalized gradient approximation made simple, *Physical Review Letters* **77**, 3865 (1996).
- [56] L. A. Agapito, S. Curtarolo, and M. Buongiorno Nardelli, Reformulation of DFT+U as a pseudohybrid Hubbard density functional for accelerated materials discovery, *Physical Review X* **5**, 011006 (2015).
- [57] M. Buongiorno Nardelli, F. T. Cerasoli, M. Costa, S. Curtarolo, R. D. Gennaro, M. Fornari, L. Liyanage, A. R. Supka, and H. Wang, PAOFLOW: A utility to construct and operate on ab initio Hamiltonians from the projections of electronic wavefunctions on atomic orbital bases, including characterization of topological materials, *Computational Materials Science* **143**, 462 (2018).
- [58] F. T. Cerasoli, A. R. Supka, A. Jayaraj, M. Costa, I. Siloi, J. Sławińska, S. Curtarolo, M. Fornari, D. Ceresoli, and M. Buongiorno Nardelli, Advanced modeling of materials with PAOFLOW 2.0: New features and software design, *Computational Materials Science* **200**, 110828 (2021).
- [59] L. A. Agapito, S. Ismail-Beigi, S. Curtarolo, M. Fornari, and M. Buongiorno Nardelli, Accurate tight-binding Hamiltonian matrices from ab initio calculations: Minimal basis sets, *Physical Review B* **93**, 035104 (2016).
- [60] L. A. Agapito, M. Fornari, D. Ceresoli, A. Ferretti, S. Curtarolo, and M. Buongiorno Nardelli, Accurate tight-binding Hamiltonians for two-dimensional and layered materials, *Physical Review B* **93**, 125137 (2016).